# Proton single-particle states in 21,23Na through the (d,n) reaction

# Proton single-particle states in $^{21,23}$Na through the $(d,n)$ reaction

A. Terakawa, T. Tohei, T. Nakagawa, A. Sato,* J. Takamatsu,† M. Mori,‡ and A. Narita
*Department of Physics, Tohoku University, Sendai, 980 Japan*

H. Orihara, K. Ishii, T. Niizeki,§ M. Oura,‖ S. Hirasaki,¶ M. Hosaka, and G. C. Jon**
*Cyclotron and Radioisotope Center, Tohoku University, Sendai, 980 Japan*

K. Miura
*Tohoku Institute of Technology, Sendai, 982 Japan*

H. Ohnuma
*Department of Physics, Tokyo Institute of Technology, Oh-okayama, Tokyo, 152 Japan*
(Received 23 November 1992)

Proton single-particle states in $^{21,23}$Na were studied through the $(d,n)$ reaction on $^{20,22}$Ne at $E_d=25$ MeV. Angular distributions of the emitted neutrons leading to the final states up to $E_x=15$ MeV were measured. Spectroscopic information has been obtained from an analysis with the adiabatic deuteron breakup approximation, where $s$-wave deuteron breakup effects have been included. Proton unbound transitions were analyzed by means of Vincent and Fortune's method. It was found that the observed proton single-particle states in $^{21,23}$Na exhausted almost all the strength for the $2s1d$ shell. The distributions of the $2s1d$ strength were reasonably reproduced by recent $2s1d$ shell model calculations. The occupation probabilities and single-particle energies of the proton orbits near Fermi levels in the ground states of $^{20,22}$Ne were deduced in a framework of combined analysis of the stripping and pickup data on the same target nucleus.

PACS number(s): 21.10.Pc, 25.45.Hi, 27.30.+t

## I. INTRODUCTION

The one-nucleon transfer reaction plays an important role in studies of the single-particle or single-hole states in residual nuclei and ground-state properties of the target nucleus, such as the occupation probability and single-particle energy of the shell model orbit. The proton single-particle properties of low-lying states in $^{21,23}$Na have been investigated through the $(d,n)$ reaction [1–3] at $E_d<10$ MeV and the ($^3$He,$d$) reaction [4,5] at $E_h<15$ MeV. Previous studies have revealed the proton single-particle strength in the low excitation region of $^{21,23}$Na. However, the spectroscopic strengths obtained in these experiments may suffer from contributions from the compound nuclear formation process, since their incident energies are rather low.

Recently, high-resolution experiments for the quasielastic $(e,e'p)$ reaction have been carried out [6,7] to derive the proton occupancy for the specific orbits of nuclei in a less model-dependent manner. Since the electron-induced proton knockout reaction probes different parts of the bound-state wave function and proceeds through a different reaction mechanism, it provides information complementary to hadronic one-nucleon-transfer reactions. For $sd$-shell nuclei, Wesseling *et al.* have recently carried out such a high-resolution $(e,e'p)$ measurement on $^{30}$Si, $^{31}$P, and $^{32}$S [7]. One of their remarks is that a comparison of their results to those obtained with the proton pickup reaction shows large differences in the deduced spectroscopic factors. The theoretical description of both hadronic and leptonic reactions seems not yet adequate to determine absolute spectroscopic factors.

$2s1d$ shell nuclei have received considerable attention from the theoretical side as well. Shell model calculations on basis of the complete $2s1d$ shell model space have been developed by Wildenthal [8]. Properties of individual states in $A=17-39$ mass nuclei have been studied using these wave functions. In the present study we aim to test the $2s1d$ shell model wave functions by comparing theoretical predictions with experimental results, where most strengths over the $2s1d$ shell are expected to be covered in the probed excitation range of $E_x=0-15$ MeV corresponding to the energy of $<1\hbar\omega$ ($40A^{-1/3}$ MeV) in this mass region.

*Present Address: C&C Information Technology Research Laboratories, NEC Co., Ltd. Kawasaki, 216 Japan.
†Present Address: ULSI Research Center, Toshiba Co., Ltd. Kawasaki, 210 Japan.
‡Present Address: NEC Software Niigata, Ltd. Niigata, Japan.
§Present Address: Department of Physics, Tokyo Institute of Technology, Oh-okayama, Tokyo, 152 Japan.
‖Present Address: The Institute of Physical and Chemical Research (RIKEN), Wako, Saitama, 351-01 Japan.
¶Present Address: NIKKEI Shinbunn Co., Ltd. Tokyo, 100 Japan.
**Present Address: Institute of Physics, ACADEMIA SINICA, Taipei, Taiwan 11529, The Republic of China.

 

Furthermore, we aim to deduce the occupation probabilities and single-particle energies of proton orbits near Fermi levels in the ground states of $^{20,22}$Ne. It is predicted [9–11] that the occupation probability is strongly affected by nucleon-nucleon correlations, such as long-range, tensor, and short-range correlations. In addition, pairing correlations may also be important for the open-shell nuclei. Hence, the precise determination of the occupation probability leads to a test of the nuclear many-body theory. In order to deduce the occupation probability and single-particle energy in the present work, we perform a combined analysis [12,13] of stripping and pickup data on the same target nucleus, thus canceling uncertainties in the distorted-wave analyses.

In this paper we present the study of the $^{20,22}$Ne$(d,n)^{21,23}$Na reactions carried out in the course of a systematic investigation of the $(d,n)$ reaction at $E_d=25$ MeV [14,15]. The $(d,n)$ reaction at a sufficiently high incident energy may be a powerful tool for probing the proton single-particle properties of nuclei since the theoretical treatment for this reaction is more straightforward than those for other proton stripping reactions.

## II. EXPERIMENTAL PROCEDURE

Experiments were performed using a 25-MeV deuteron beam from the $K=50$ MeV AVF cyclotron at the Cyclotron and Radioisotope Center (CYRIC), Tohoku University. Neutron energies were measured by the time-of-flight (TOF) technique. Twelve neutron detectors containing the liquid scintillator NE213 were set at a flight path of 44 m from the target, where the effective detection solid angle was 0.23 msr. Angular distributions of the emitted neutrons were measured using a beam swinger system. Detector efficiency was 3%, which was determined by the $^7$Li$(p,n)^7$Be reaction through activation analysis. Details of the CYRIC TOF facility have been described elsewhere [16,17].

$^{20,22}$Ne gases isotopically enriched to 99.9% were used as targets. These gases were filled in a 2-cm-long (along with the beam direction) and 20-mm $\phi$ gas cell with 10-mg/cm$^2$-thick platinum windows. Target thicknesses were 1.0 and 1.1 mg/cm$^2$ for $^{20}$Ne and $^{22}$Ne, respectively. In addition, in the backward-angle ($\theta_{\rm lab}\geq 30°$) measurements for the $^{20}$Ne$(d,n)^{21}$Na reaction, a 25-cm-long and 30-mm $\phi$ gas cell with 10-$\mu$m Havar foil windows was used. This arrangement made it possible to mask the neutrons emitted from window foils from detectors by a 1-m-thick concrete shield. For this type of the gas cell, however, the target thickness depended on the neutron detection angle: it ranged from 3.4 to 6.3 mg/cm$^2$ for $^{20}$Ne in the angular range of $\theta_L=40°-75°$. This latter large-volume gas cell was not used for the $^{22}$Ne$(d,n)^{23}$Na reaction, since $^{22}$Ne gas was more expensive.

Typical neutron excitation energy spectra for the $^{20,22}$Ne$(d,n)^{21,23}$Na reactions are shown in Figs. 1 and 2, respectively. Overall energy resolutions for the neutrons leading to the low-lying states in the residual nuclei were 170 keV for the disk-type cell, and 200 keV for the cylindrical one. The spectrum in Fig. 1 was obtained by a cylindrical gas cell, while that in Fig. 2 was obtained by a disk-type one. Solid lines are results of a peak-fitting analysis, where Gaussian shapes and a smooth background function are assumed. Several peaks are added around peaks of interest in order to obtain reasonable peak-fitting results, though the angular distributions were not sufficient to assign $l$ value for peaks for which the excitation energy is not labeled in the figures. The error on the excitation energies is $\pm 10$ keV for prominent peaks, while it is $\pm 30$ keV for weakly populated ones. Gamma-ray events have been rejected by the pulse-shape discrimination technique. Backgrounds in the case of the disk-type cell are mainly due to the neutrons from the platinum windows. Neutron yields for the two gas cells were consistent for strongly populated peaks. Errors in the absolute magnitudes of cross sections are estimated to be less than 15%, the dominant part of which is due to the uncertainty of the detector efficiency.

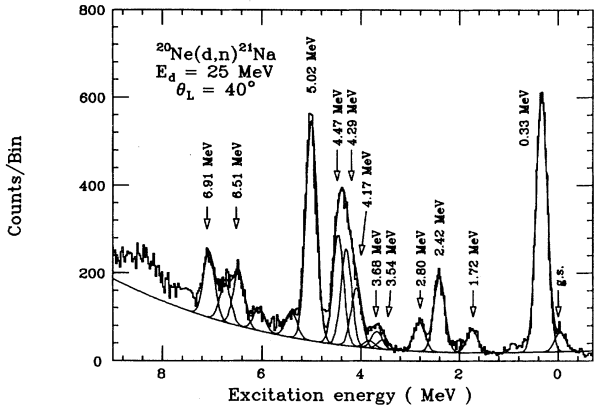


FIG. 1. Neutron spectrum of the $^{20}$Ne$(d,n)^{21}$Na reaction at $\theta_L=40°$ obtained using the cylindrical type of gas cell. Solid lines are results of a peak-fitting analysis, where Gaussian shapes and a smooth background line are assumed. Energy per bin is 25 keV.

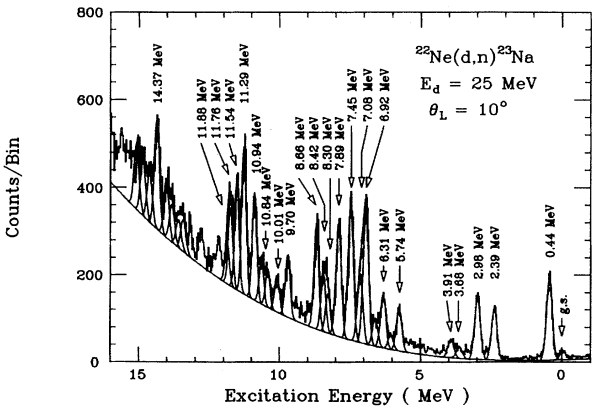


FIG. 2. Neutron spectrum of the $^{22}$Ne$(d,n)^{23}$Na reaction at $\theta_L=10°$ obtained using the disk-type gas cell. Solid lines are results of a peak-fitting analysis, where Gaussian shapes and a smooth background line are assumed. Energy per bin is 25 keV.

TABLE I. Potential parameters used in the present analyses.

| | $V_r$ (MeV) | $r_r$ (fm) | $a_r$ (fm) | $W_v$ (MeV) | $r_{iv}$ (fm) | $a_{iv}$ (fm) | $W_s$ (MeV) | $r_{is}$ (fm) | $a_{is}$ (fm) | $V_{so}$ (MeV) | $r_{so}$ (fm) | $a_{so}$ (fm) | $r_c$ (fm) | NL (fm) |
|---|---|---|---|---|---|---|---|---|---|---|---|---|---|---|
| $^{20}$Ne+$d$ | | | | | | | | | | | | | | |
| ADBA[a] | 98.90 | 1.17 | 0.779 | | | | 16.20 | 1.320 | 0.546 | 6.20 | 1.01 | 0.750 | 1.30 | 0.43 |
| DWBA[b] | 85.37 | 1.17 | 0.751 | 0.75 | 1.325 | 0.705 | 12.09 | 1.325 | 0.705 | 6.62 | 1.07 | 0.660 | 1.30 | 0.54 |
| $^{21}$Na+$n$ | 47.65 | 1.17 | 0.750 | 2.48 | 1.320 | 0.477 | 6.48 | 1.320 | 0.477 | 6.20 | 1.01 | 0.750 | | 0.85 |
| $^{20}$Ne+$p$ | c | 1.25 | 0.650 | | | | | | | $\lambda=25$ | 1.25 | 0.650 | 1.25 | |
| $^{20}$Ne+$d$ | | | | | | | | | | | | | | |
| ADBA[a] | 98.90 | 1.17 | 0.779 | | | | 16.40 | 1.320 | 0.605 | 6.20 | 1.01 | 0.750 | 1.30 | 0.43 |
| DWBA[b] | 85.28 | 1.17 | 0.751 | 0.75 | 1.325 | 0.725 | 12.09 | 1.325 | 0.725 | 6.62 | 1.07 | 0.660 | 1.30 | 0.54 |
| $^{23}$Na+$n$ | 43.24 | 1.17 | 0.750 | 3.96 | 1.320 | 0.540 | 3.72 | 1.320 | 0.540 | 6.20 | 1.01 | 0.750 | | 0.85 |
| $^{20}$Ne+$p$ | c | 1.25 | 0.650 | | | | | | | $\lambda=25$ | 1.25 | 0.650 | 1.25 | |

[a]Potential parameters used in the adiabatic deuteron breakup approximation calculations.
[b]Potential parameters taken from Ref. [22].
[c]The well depth is adjusted to reproduce the respective separation energies.

## III. DISTORTED-WAVE ANALYSIS

Angular distributions of the differential cross section were analyzed with the adiabatic deuteron breakup approximation (ADBA) [18], where $s$-wave deuteron breakup effects have been included, as well as with the conventional treatment of the distorted-wave Born approximation (DWBA). The calculations were performed with the code DWUCK4 [19]. Finite range and nonlocality corrections were included in the analysis. The adiabatic deuteron potential was derived from the set of nucleon potentials at $E_p=E_n=1/2E_d$, which have been given by Becchetti and Greenlees [20] for protons and by Carlson, Zafiratos, and Lind [21] for neutrons. In the conventional DWBA treatment the deuteron optical potential parameters were taken from the global sets of Daehnick *et al.* [22]. The single-particle wave function for the transferred proton was generated by the separation energy method with the Woods-Saxon potential. The potential parameters, and finite range and nonlocality parameters are listed in Table I. The form factors for the proton unbound transitions were calculated by means of Vincent and Fortune's method [23].

Experimental spectroscopic factors $S$ are extracted from the following equation:

$$\left[\frac{d\sigma}{d\Omega}\right]_{\text{expt}} = 1.55\frac{2J_f+1}{2J_i+1}\frac{C^2S}{2j+1}\left[\frac{d\sigma}{d\Omega}\right]_{\text{DWUCK}}, \quad (1)$$

where $J_i$ and $J_f$ are the spins of initial and final states, respectively, and $j$ is the total angular momentum of the transferred particle. $C$ is an isospin Clebsh-Gordan coefficient. The values of $C^2$ are unity for the $^{20}$Ne$(d,n)^{21}$Na reaction, and $\frac{2}{3}$ and $\frac{1}{3}$ for the $T=\frac{1}{2}$ and $\frac{3}{2}$ states, respectively, in the $^{22}$Ne$(d,n)^{23}$Na reaction.

Typical angular distributions for each transferred orbital angular momentum are illustrated in Fig. 3 together with the theoretical predictions. Solid lines represent results of the ADBA calculation, while dashed lines those of the conventional DWBA calculation. In general, good agreement between the experimental and theoretical results has been obtained as far as the shape of the cross sections at forward angles ($\theta_L < 50°$) is concerned, though agreement is rather poor for the case of the $l=1$ transition, where $l$ denotes angular momentum of the transferred single particle. The spectroscopic strengths

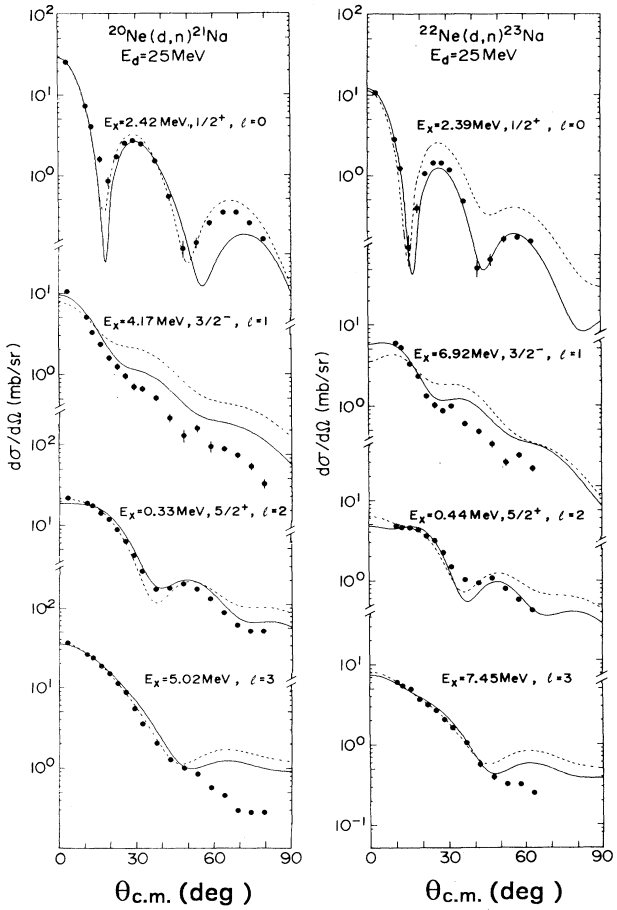


FIG. 3. Comparisons between the experimental and theoretical angular distributions for the different $l$ transitions. Solid lines represent results of ADBA calculations and dashed lines show those of conventional DWBA calculations.

TABLE II. Spectroscopic strengths obtained using the two different potential parameters.

| $E_x$ (MeV) | $J^\pi$ | $l$ | $(2J_f+1)C^2S$ ADBA[a] | DWBA[b] |
|---|---|---|---|---|
| | $^{20}$Ne$(d,n)^{21}$Na | | | |
| 0.33 | $\frac{5}{2}^+$ | 2 | 3.76 | 3.55 |
| 2.42 | $\frac{1}{2}^+$ | 0 | 1.93 | 2.01 |
| 4.17 | $\frac{3}{2}^-$ | 1 | 0.85 | 0.85 |
| 5.02 | $(\frac{7}{2}^-)$ | 3 | 3.23 | 3.01 |
| | $^{22}$Ne$(d,n)^{23}$Na | | | |
| 0.44 | $\frac{5}{2}^+$ | 2 | 2.91 | 2.44 |
| 2.39 | $\frac{1}{2}^+$ | 0 | 0.50 | 0.60 |
| 6.92 | $\frac{3}{2}^-$ | 1 | 0.53 | 0.49 |
| 7.45 | $(\frac{7}{2}^-)$ | 3 | 1.62 | 1.55 |

[a]The results obtained with the adiabatic deuteron potential.
[b]The results obtained with the global potential taken from Ref. [22].

$(2J_f+1)C^2S$ derived by the two types of analysis are compared in Table II. It is worth pointing out that there are no significant differences in the spectroscopic strengths. This is consistent with the results of our systematic study [14,15] of the 25-MeV $(d,n)$ reaction on $2s1d$ shell nuclei. We adopt the ADBA analysis in the following discussions, since it gives, in general, a better description of the angular distributions.

## IV. RESULTS AND DISCUSSION

### A. $^{20}$Ne$(d,n)^{21}$Na reaction

$l$ assignments have been made for 11 transitions leading to states up to $E_x=7$ MeV in $^{21}$Na. The differential cross sections for the individual states are shown in Figs. 4 and 5 along with the ADBA predictions. Obtained spectroscopic information is listed in Table III together with that previously reported for $A=21$ system [1,2,24]. The spectroscopic strengths of the proton unbound states ($E_x>2.43$ MeV) have not been reported in the previous work.

It is generally believed that the value of the spectroscopic factor with single proton transfer reactions, compared to that with $(e,e'p)$ knock-out experiment, is more sensitive to the shape of the single-particle binding potential or to the optical-model potential with which DWBA calculation is carried out. In this sense, the spectroscopic factors from nucleon transfer reactions have to be considered as relative ones. The strength distributions for the positive-parity states in $^{21}$Na are shown in Fig. 6 together with the predictions by the $2s1d$ shell model [8]. The shell model calculation has been performed using the code OXBASH [25]. The comparison seems satisfactory.

#### *1. Positive-parity states*

$1d_{5/2}$ transition strength has been observed to the 0.33-, 3.54-, and 4.29-MeV states. The result of the

TABLE III. Experimental spectroscopic strengths in the $A=21$ system.

| $^{21}$Na | | $(d,n)$, $E_d=25$ MeV[b] | | | $(d,n)$, $E_d=5.2$ MeV[c] | | | $(d,n)$, $E_d=5.9$ MeV[d] | | | $^{21}$Ne | | $(d,p)$, $E_d=16$ MeV[e] | | |
|---|---|---|---|---|---|---|---|---|---|---|---|---|---|---|---|
| $E_x$ (MeV)[a] | $J^\pi$[a] | $l$ | $nlj$ | $(2J_f+1)C^2S$ | $l$ | $nlj$ | $(2J_f+1)C^2S$ | $l$ | $nlj$ | $(2J_f+1)C^2S$ | $E_x$ (MeV)[a] | $J^\pi$[a] | $l$ | $nlj$ | $(2J_f+1)C^2S$ |
| G.S. | $\frac{3}{2}^+$ | | | | | | | | | | G.S. | $\frac{3}{2}^+$ | | $1d_{3/2}$ | $\leq 0.11$ |
| 0.33 | $\frac{5}{2}^+$ | 2 | $1d_{5/2}$ | 3.76 | 2 | $1d_{5/2}$ | 2.4 | 2 | $1d_{5/2}$ | 2.1 | 0.35 | $\frac{5}{2}^+$ | 2 | $1d_{5/2}$ | 3.7 |
| 2.42 | $\frac{1}{2}^+$ | 0 | $2s_{1/2}$ | 1.93 | 0 | $2s_{1/2}$ | 0.46 | 0 | $2s_{1/2}$ | 0.9 | 2.79 | $\frac{1}{2}^+$ | 0 | $2s_{1/2}$ | 0.90 |
| 2.80 | $\frac{1}{2}^-$ | 1 | $1p_{1/2}$ | 0.26 | | | | | | | 3.74 | $\frac{5}{2}^+$ | 2 | $2d_{5/2}$ | 0.20 |
| 3.54 | $\frac{5}{2}^+$ | 2 | $1d_{5/2}$ | 0.16 | | | | | | | 4.53 | $\frac{5}{2}^+$ | 2 | $1d_{5/2}$ | 0.78 |
| 3.68 | $\frac{3}{2}^-$ | 1 | $1p_{3/2}$ | 0.20 | | | | | | | 4.68 | $\frac{3}{2}^+$ | | | |
| 4.17 | $\frac{3}{2}^-$ | 1 | $2p_{3/2}$ | 0.85 | | | | | | | 4.73 | $\frac{3}{2}^-$ | 1 | $2p_{3/2}$ | 2.3 |
| 4.29 | $\frac{5}{2}^+$ | 2 | $1d_{5/2}$ | 1.29 | | | | | | | 5.34 | $\frac{7}{2}^-$ | 2 | $1d_{3/2}$ | 1.1 |
| 4.47 | $\frac{3}{2}^+$ | 2 | $1d_{3/2}$ | 1.44 | | | | | | | 5.55 | $\frac{3}{2}^+$ | 2 | $1d_{3/2}$ | 0.57 |
| 5.02 | | 3 | $1f_{7/2}$ | 3.23 | | | | | | | 5.82 | $\frac{3}{2}^+$ | 2 | $1d_{3/2}$ | 0.28 |
| 6.51 | $\frac{3}{2}^+$ | 2 | $1d_{3/2}$ | 0.71 | | | | | | | 6.61 | $(\frac{3}{2},\frac{5}{2})^+$ | 2 | $1d_{5/2}$ | 1.1 |
| 6.91 | $(\frac{3}{2}^+)$ | 2 | $1d_{3/2}$ | 0.44 | | | | | | | | | | | |

$\sum(2J_f+1)C^2S(1p_{3/2})=0.20$
$\sum(2J_f+1)C^2S(1p_{1/2})=0.26$
$\sum(2J_f+1)C^2S(1d_{5/2})=5.21$
$\sum(2J_f+1)C^2S(2s_{1/2})=1.93$
$\sum(2J_f+1)C^2S(1d_{3/2})=2.59$
$\sum(2J_f+1)C^2S(1f_{7/2})=3.23$
$\sum(2J_f+1)C^2S(2p_{3/2})=0.85$

[a]References [26,27].
[b]Present work.
[c]Reference [1].
[d]Reference [2].
[e]Reference [24].

analysis shows that large amounts of the $1d_{5/2}$ strength is located in the 0.33-MeV state. The spectroscopic strength for this state is in good agreement with that for the mirror state in $^{21}$Ne obtained from the $(d,p)$ reaction [24], as can be seen from Table III.

The transition leading to the 2.42-MeV, $\frac{1}{2}^+$ state is the only $l=0$ transition observed in the present measurement. In addition, the spectroscopic strength derived for this state corresponds to about 97% of the sum-rule limit for $2s_{1/2}$ transfer.

The strength distribution for the $1d_{3/2}$ orbit shows a fragmentation of the strength over the 4.47-, 6.51-, and 6.91-MeV states. The high-lying $1d_{3/2}$ strength at $E_x > 7$ MeV predicted by the shell model has not been identified in the present work due to the background.

The experimental strength distributions for the $1d_{5/2}$ and $2s_{1/2}$ orbits are successfully reproduced by the $2s1d$ shell model, while there seems to be a slight disagreement in the case of the $1d_{3/2}$ strength, as can be seen from Fig. 6.

### 2. *Negative-parity states*

Low-lying negative-parity states in lighter $2s1d$ shell nuclei are known to be excited in the one-nucleon pickup reaction [26,27]. Therefore, these negative-parity states

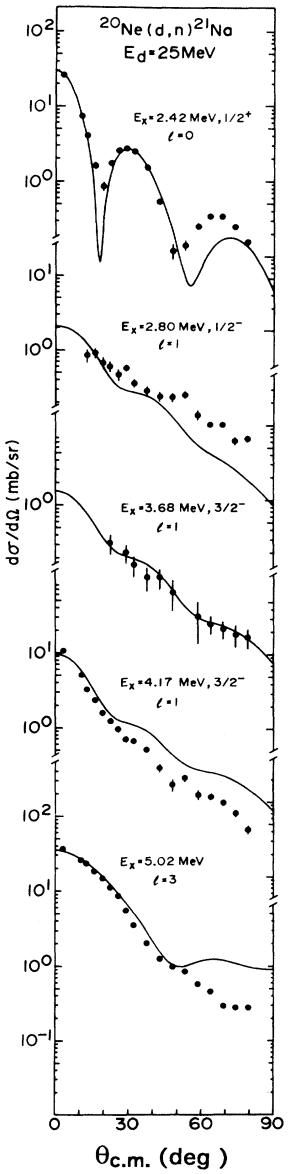


FIG. 4. Differential cross sections for the $l=0$, 1, and 3 transitions in the $^{20}$Ne$(d,n)^{21}$Na reaction. Solid lines represent the results of the ADBA calculations.

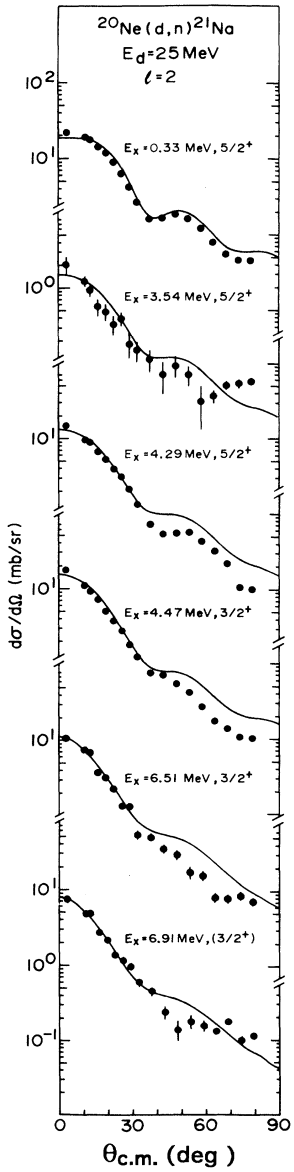


FIG. 5. Differential cross sections for the $l=2$ transitions in the $^{20}$Ne$(d,n)^{21}$Na reaction. Solid lines represent results of the ADBA calculations.

are considered to have a $1p$ single-hole character. In $^{21}$Na, the 2.80- and 3.68-MeV states are the lowest $\frac{1}{2}^-$ and $\frac{3}{2}^-$ states, and their mirror states in $^{21}$Ne have strongly been populated in the one-neutron pickup reactions on $^{22}$Ne [28–30]. This suggests that the 2.80- and 3.68-MeV states in $^{21}$Na have the $(\pi 2s\,1d)4(\pi 1p)^{-1}$ hole configuration. In the presently measured proton stripping reaction, these states are indeed weakly populated as seen in Fig. 1. This suggests that there exists a six-particle–two-hole component, such as the $(2s\,1d)^6(1p)^{-2}$ configuration, in the ground-state wave function of $^{20}$Ne. On the other hand, a strong $l=1$ transition leading to the 4.17-MeV, $\frac{3}{2}^-$ state, the mirror states of which in $^{21}$Ne at 4.73 MeV has particle character as is dominantly populated by the neutron stripping reaction [26,27], but is not strongly excited by the neutron pickup reaction [26,27], may be due to $2p_{3/2}$ proton transfer. The deduced spectroscopic strength of 0.85 corresponds to about 21% of the total $2p_{3/2}$ strength.

No $l=3$ has so far been reported [26,27] in the one-proton stripping reaction on $^{20}$Ne. In a systematic study of the $(d,n)$ reaction on $sd$-shell nuclei [14,15], however, we have observed strong $l=3$ transitions in almost all cases investigated; i.e., leading to a 6.93-MeV state in $^{19}$F by the $(d,n)$ reaction on $^{18}$O, to 3.70 MeV in $^{25}$Al, etc. In the present study, we have a candidate of $l=3$ transition as a prominent peak leading to the 5.02-MeV state as seen in Fig. 1, though it is difficult to eliminate completely the possibility for $l=2$ transition by the shape of the angular distribution shown in Fig. 4. If we assume this transition to be $l=2$ leading to a $\frac{3}{2}^+$ state, we obtain the spectroscopic factor of 3.23, by which the summed value is 5.82, being unreasonably large in its magnitude com-

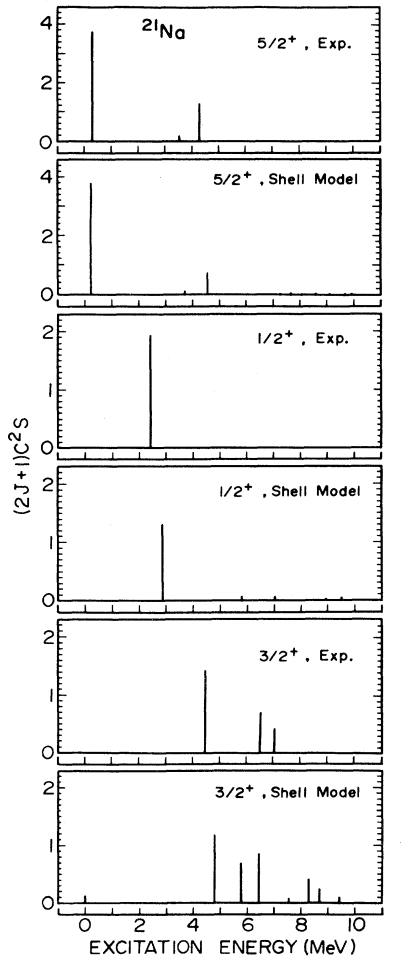


FIG. 6. Comparisons between experimental $2s\,1d$ strength distributions in $^{21}$Na and shell model predictions.

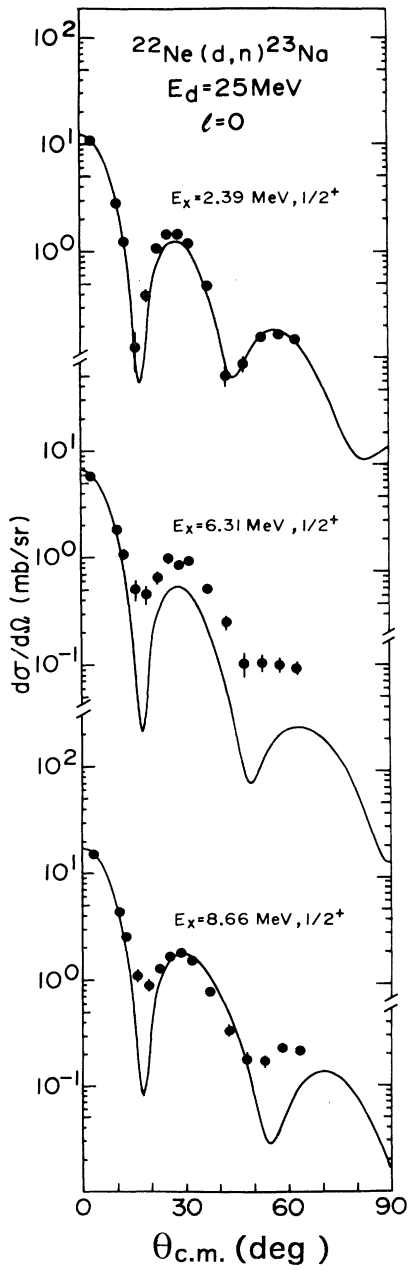


FIG. 7. Differential cross sections for the $l=0$ transitions in the $^{22}$Ne$(d,n)^{23}$Na reaction. Solid lines represent results of the ADBA calculations.

paring with the sum-rule limit of 4. Thus, it is highly improbable to assign this transition to the 5.02-MeV state to be a $1d_{3/2}$ transfer. Assuming the $1f_{7/2}$ transfer, we obtain spectroscopic strength of about 40% of the $1f_{7/2}$ sum-rule limit, which is a quite reasonable result from systematic behavior of the $1f_{7/2}$ strength in this mass region [14,15].

### B. $^{22}$Ne$(d,n)^{23}$Na reaction

$l$ assignments have been made for 24 transitions leading to states up to $E_x = 14.4$ MeV in $^{23}$Na. The spectroscopic results for $^{23}$Na are summarized in Table IV. The observed angular distributions are illustrated in Figs. 7–10. The strength distributions for the $2s\,1d$ orbits are compared with those by the shell model [8] in Fig. 11. In previous work [3–5], the spectroscopic information for the proton unbound states ($E_x > 8.79$ MeV) has not been reported. Furthermore, no strong $l=3$ transition has hitherto been reported. In the present work, however, several strong $l=3$ transitions have been observed for the first time, resolving the missing $1f_{7/2}$ strength problem in $^{23}$Na. As for the 14.37-MeV state, it is located too far from the threshold for proton emission. The spectroscopic strength for this state is less reliable.

#### *1. Positive-parity states*

The 0.44-MeV, $\frac{5}{2}^+$ state is strongly populated in the neutron spectrum as can be seen from Fig. 2 The spec-

TABLE IV. Experimental spectroscopic strengths in $^{23}$Na.

| | | $(d,n)$, $E_d=25$ MeV[b] | | | $(^3\text{He},d)$, $E_h=10$, 12 MeV[c] | | | $(^3\text{He},d)$, $E_h=15$ MeV[d] | | | $(d,n)$, $E_d=5.5$ MeV[e] | | |
|---|---|---|---|---|---|---|---|---|---|---|---|---|---|
| $E_x$ (MeV)[a] | $J^\pi;T$[a] | $l$ | $nlj$ | $(2J_f+1)C^2S$ | $l$ | $nlj$ | $(2J_f+1)C^2S$ | $l$ | $nlj$ | $(2J_f+1)C^2S$ | $l$ | $nlj$ | $(2J_f+1)C^2S$ |
| G.S. | $\frac{3}{2}^+$ | (2) | $1d_{3/2}$ | (0.33) | | | | 2 | $1d_{3/2}$ | 0.32 | 2 | $1d_{3/2}$ | (1.09) |
| 0.44 | $\frac{5}{2}^+$ | 2 | $1d_{5/2}$ | 2.91 | | | | 2 | $1d_{5/2}$ | 2.10 | 2 | $1d_{5/2}$ | (1.28) |
| 2.39 | $\frac{1}{2}^+$ | 0 | $2s_{1/2}$ | 0.50 | 0 | $2s_{1/2}$ | 0.73 | 0 | $2s_{1/2}$ | 0.50 | 0 | $2s_{1/2}$ | 0.28 |
| 2.64 | $\frac{1}{2}^-$ | | | | (1) | $1p_{1/2}$ | 0.03 | 1 | $1p_{1/2}$ | 0.043 | | | |
| 2.98 | $\frac{3}{2}^+$ | 2 | $1d_{3/2}$ | 1.68 | 2 | $1d_{3/2}$ | 0.87 | 2 | $1d_{3/2}$ | 1.28 | 2 | $1d_{3/2}$ | 0.69 |
| 3.68 | $\frac{3}{2}^-$ | 1 | $1p_{3/2}$ | 0.15 | 1 | $1p_{3/2}$ | 0.07 | 1 | $1p_{3/2}$ | 0.076 | 1 | $1p_{3/2}$ | 0. |
| 3.91 | $\frac{5}{2}^+$ | 2 | $1d_{5/2}$ | 0.39 | (2) | $1d_{5/2}$ | 0.30 | 2 | $1d_{5/2}$ | 0.27 | | | |
| 5.74 | $\frac{5}{2}^+$ | 2 | $1d_{5/2}$ | 0.47 | (2) | $1d_{5/2}$ | $\leq 0.37$ | 2 | $1d_{5/2}$ | 0.21 | (2) | $1d_{5/2}$ | 0.20 |
| 6.31 | $\frac{1}{2}^+$ | 0 | $2s_{1/2}$ | 0.27 | 0 | $2s_{1/2}$ | 0.50 | 0 | $2s_{1/2}$ | 0.27 | 0 | $2s_{1/2}$ | 0.18 |
| 6.92 | $\frac{3}{2}^-$ | 1 | $2p_{3/2}$ | 0.53 | (1) | $2p_{3/2}$ | $\leq 0.80$ | 1 | $2p_{1/2}$ | 0.30 | 1 | $2p_{3/2}$ | 0.19 |
| 7.08 | $\frac{3}{2}^-$ | 1 | $2p_{3/2}$ | 0.31 | 1 | $2p_{3/2}$ | 0.40 | 1 | $2p_{1/2}$ | 0.17 | 1 | $2p_{3/2}$ | 0.08 |
| 7.45 | $\frac{5}{2}^+$ | 3 | $1f_{7/2}$ | 1.62 | (2) | $1d_{3/2}$ | $\leq 0.73$ | 2 | $1d_{3/2}$ | 0.58 | 1 | $2p_{3/2}$ | 0.11 |
| 7.89 | $\frac{5}{2}^+;\frac{3}{2}$ | 2 | $1d_{5/2}$ | 0.87 | (2 or 3 ) | $1d_{5/2}$ | 0.20 | 2 | $1d_{5/2}$ | 0.46 | 2 | $1d_{5/2}$ | 0.40 |
| 8.30 | | 3 | $1f_{7/2}$ | 0.44 | | | | 3,(2) | $1f_{5/2}$ | 0.49 | | | |
| 8.42 | $\frac{3}{2}^+$ | 2 | $1d_{3/2}$ | 0.52 | | | | (2) | $1d_{5/2}$ | 0.18 | (3) | $1f_{5/2}$ | 0.16 |
| 8.66 | $\frac{1}{2}^+;\frac{3}{2}$ | 0 | $2s_{1/2}$ | 1.16 | 0 | $2s_{1/2}$ | 0.21 | 0 | $2s_{1/2}$ | 0.54 | 1 | $2s_{1/2}$ | 0.50 |
| 9.70 | $\frac{3}{2}^+$ | 2 | $1d_{3/2}$ | 0.32 | | | | | | | | | |
| 10.01 | $\frac{5}{2}^+$ | 2 | $1d_{5/2}$ | 0.19 | | | | | | | | | |
| 10.84[b] | | (1) | $2p_{3/2}$ | 0.35 | | | | | | | | | |
| 10.94[b] | | 2 | $1d_{3/2}$ | 0.42 | | | | | | | | | |
| 11.29[b] | | 2 | $1d_{3/2}$ | 0.71 | | | | | | | | | |
| 11.54[b] | | 3 | $1f_{7/2}$ | 0.49 | | | | | | | | | |
| 11.76[b] | | 3 | $1f_{7/2}$ | 0.40 | | | | | | | | | |
| 11.88[b] | | 3 | $1f_{7/2}$ | 0.24 | | | | | | | | | |
| 14.37[b] | | 3 | | | | | | | | | | | |

$\sum(2J_f+1)C^2S(1p_{3/2}) = 0.15$
$\sum(2J_f+1)C^2S(1d_{5/2}) = 4.83$
$\sum(2J_f+1)C^2S(2s_{1/2}) = 1.93$
$\sum(2J_f+1)C^2S(1d_{3/2}) = 3.98$
$\sum(2J_f+1)C^2S(1f_{7/2}) = 3.19$
$\sum(2J_f+1)C^2S(2p_{3/2}) = 1.19$

[a]References [26,27].
[b]Present work.
[c]Refrence [4]. A correction to the original values for the factor $C^2$ ($=\frac{2}{3}$ and $\frac{1}{3}$ for $T=\frac{1}{2}$ and $\frac{3}{2}$ states, respectively) has been performed.
[d]Reference [5].
[e]Reference [3].

troscopic strength of 2.91 for this state, which is consistent with the shell model prediction, indicates that a considerable amount of $1d_{5/2}$, $T=\frac{1}{2}$ strength is exhausted by this state. The remaining $1d_{5/2}$, $T=\frac{1}{2}$ strength is located in the 3.91- and 5.74-MeV states.

Most of the $1d_{5/2}$, $T=\frac{3}{2}$ strength resides in the 7.89-MeV state which corresponds to the isobaric analog state of the ground state in $^{23}$Ne. The 10.01-MeV, $\frac{5}{2}^+$ state may be a candidate for the analog state of the 2.31-MeV state in $^{23}$Ne, since its excitation energy and spectroscopic strength of 0.19 are in good agreement with the shell model predictions [$E_x=10.10$ MeV and $(2J_f+1)C^2S=0.17$].

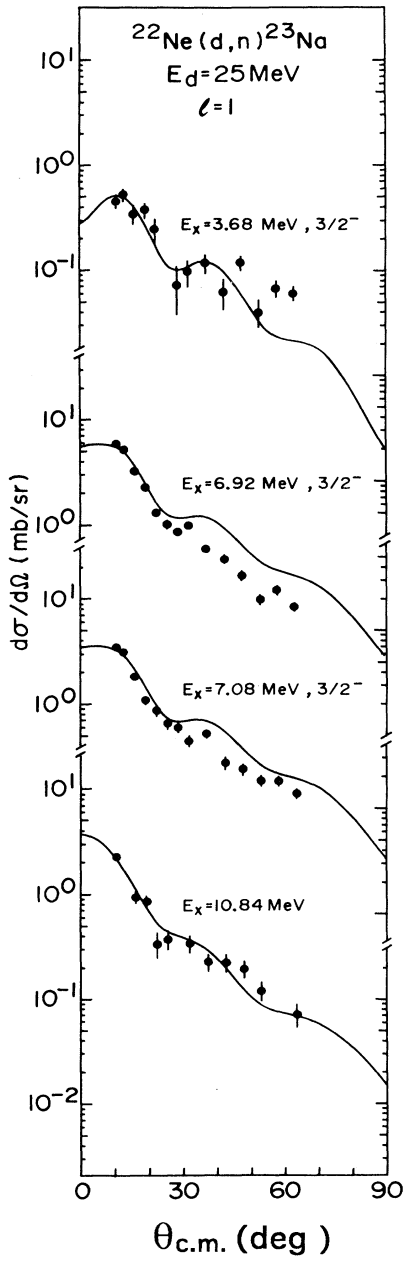


FIG. 8. Differential cross sections for the $l=1$ transitions in the $^{22}$Ne$(d,n)^{23}$Na reaction. Solid lines represent results of the ADBA calculations.

As discussed in the previous section, the $2s_{1/2}$ strength in $^{21}$Na is concentrated on the 2.42-MeV, $\frac{1}{2}^+$ state. This component for the $2s_{1/2}$ $T=\frac{1}{2}$ strength in $^{23}$Na, on the other hand, is fragmented into two $\frac{1}{2}^+$ states at 2.39 and 6.31 MeV, indicating the effects of the extra two neutrons added. The shell model completely reproduces this situation as seen in Fig. 11. Furthermore, there is a dominant $l=0$ transition leading to the 8.66-MeV state, which is the analog state of the 1.02-MeV state in $^{23}$Ne. The obtained spectroscopic strength of 1.16 for this transition is about two times as large as the total $T_>$ strength of 0.67, which is derived from the following relation [31]:

$$\sum(2J_f+1)C^2S(T_>)=\frac{\langle\text{neutron hole}\rangle}{N-Z+1}\ , \qquad (2)$$

where the angular bracket denotes the number of $2s_{1/2}$ neutron holes in the target ground state, and $N$ and $Z$ indicate, respectively, the numbers of neutrons and protons in the target nucleus. This result might be due to uncertainty of the form factor, because the proton binding energy for the 8.66-MeV state is only 130 keV. The difficulty of the theoretical treatment for the form factor has been discussed by several authors [32,33].

The $\frac{3}{2}^+$ state at 2.98 MeV is prominently populated in the neutron spectrum exhausting about 42% of the sum-rule limit. The remaining $1d_{3/2}$ strength is expected to be distributed over high-lying states. The shell model predicts that a significant fraction of the $1d_{3/2}$, $T=\frac{3}{2}$ strength may be located in the excitation region of $E_x=9-12$ MeV in $^{23}$Na. It is quite reasonable to consider that the predicted strength may reside in the states strongly populated at 9.70, 10.94, and 11.29 MeV with the characteristic $l=2$ angular distribution shape.

### 2. *Negative-parity states*

The 2.64- and 3.68-MeV states are the lowest $\frac{1}{2}^-$ and $\frac{3}{2}^-$ states in $^{23}$Na, respectively, and are strongly populated in proton pickup reactions on $^{24}$Mg [34]. Therefore, these negative-parity states have a $1p$ proton single-hole character of the $(\pi 2s1d)^4(\pi 1p)^{-1}$ configuration. We have observed the proton stripping to the 3.68-MeV state with the small strength as shown in Fig. 2. Unfortunately, the minor peak of the 2.64-MeV state is masked by the strong peaks at 2.39 and 2.98 MeV due to the limited energy resolution of the detected neutrons.

The strong $l=1$ transitions leading to the $\frac{3}{2}^-$ states at 6.92 and 7.08 MeV have also been observed with spectroscopic strengths of 0.53 and 0.31, respectively, assuming $2p_{3/2}$ transfer. The summed $2p_{3/2}$ strength in $^{23}$Na is comparable in its magnitude to that in $^{21}$Na.

We have observed a prominent peak leading to the 7.45-MeV state, for which a $J^\pi=\frac{5}{2}^+$ assignment has been given in the compilations [26,27]. However, the present study strongly suggests that the spin and parity for this state should be $\frac{7}{2}^-$. First, its angular distribution shows

a typical $l=3$ pattern as illustrated in Fig. 10. Second, if we assume $J^{\pi}=\frac{5}{2}^{+}$ for this state, the summed $1d_{5/2}$ strength surpasses the sum-rule limit, leading to the unreasonable conclusion that there may be little $1d_{5/2}$ proton occupation in the ground state of $^{22}$Ne, whereas significant fraction of the $1d_{5/2}$ proton strength has been observed in proton pickup reactions [35,36] on $^{22}$Ne.

### C. Occupation probability and single-particle energy

The spectroscopic information obtained from the one-nucleon-transfer reaction makes it possible to discuss the occupation probability $N_{nlj}$ and single-particle energy $E_{nlj}$ for the single-particle orbit in the ground state of the target nucleus. The occupation probability is expressed

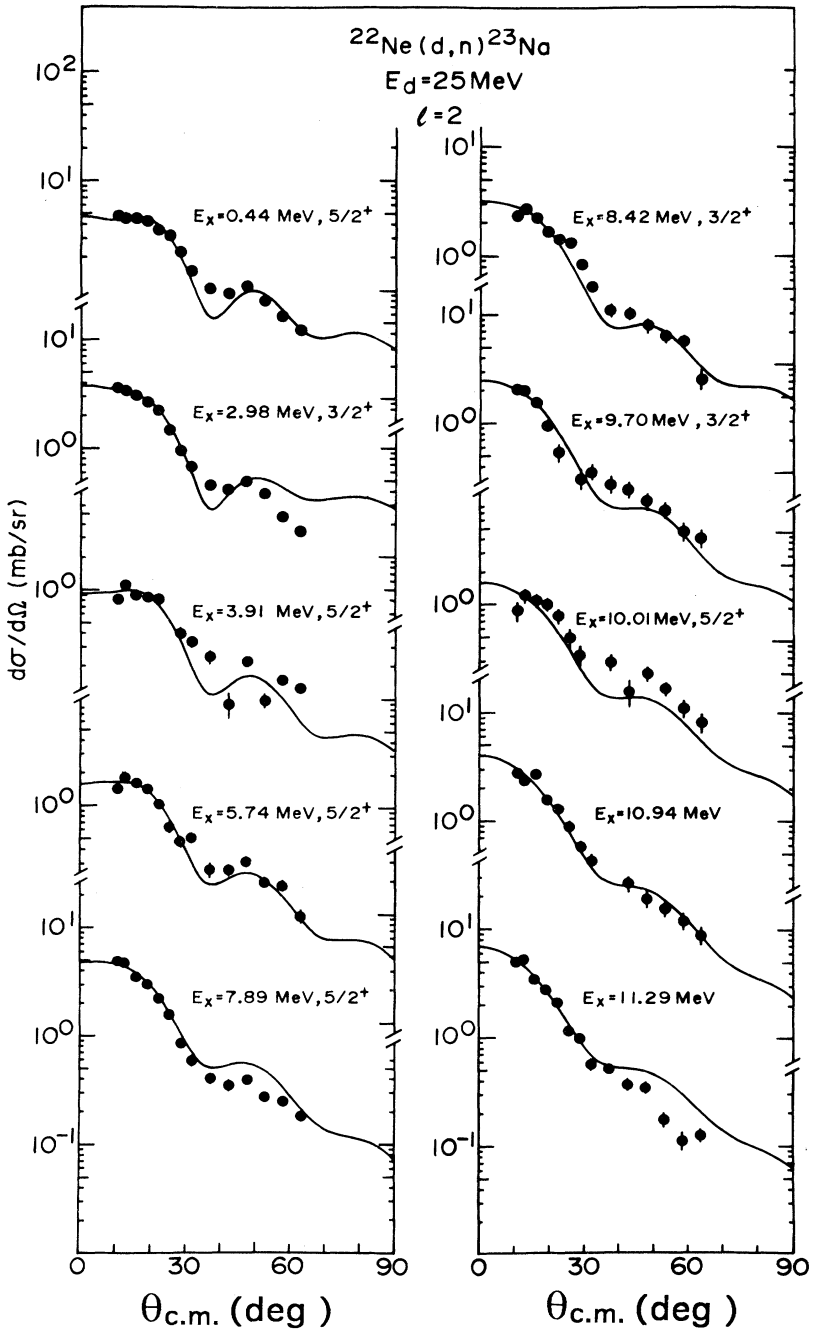


FIG. 9. Differential cross sections for the $l=2$ transitions in the $^{22}$Ne$(d,n)^{23}$Na reaction. Solid lines represent results of the ADBA calculations.

in terms of the well-known sum rule [31]

$$N_{nlj}=\frac{\sum G^{-}_{nlj}}{2j+1}=1-\frac{\sum G^{+}_{nlj}}{2j+1}\ , \tag{3}$$

where $G^{-}_{nlj}$ and $G^{+}_{nlj}$ are the spectroscopic strengths for the pickup and stripping reactions, respectively, and the summation is taken over all final states with the quantum number $nlj$. Equation (3) leads to a relation between $G^{-}_{nlj}$ and $G^{+}_{nlj}$:

$$\sum G^{-}_{nlj}+\sum G^{+}_{nlj}=2j+1\ . \tag{4}$$

This sum rule requires accurate spectroscopic factors to perform summation up to infinite excitation energy, since particle (hole) strengths may be spread over presumably due to short-range and tensor correlations. However, uncertainties encountered in the DWBA analysis allow us to extract only relative strengths. In addition, an experimentally accessible region is limited for the excitation energy in general. Recently, Grabmayr [37] has successfully determined the occupation number for the $3s_{1/2}$ proton orbital in the lead region, by developing a combined evaluation of relative spectroscopic factors and electron scattering (approach CERES), where the advantages of the different probes are explored. In the present case, however, there are no electron-scattering data for the Ne isotope, the charge density differences which allow us to perform a CERES analysis. Thus, we deduce the properties of the target ground states, as follows, by assuming that all the fragmented strengths for the single particle near the Fermi surface are located in the excitation energy region investigated in this work.

Experimental and theoretical ambiguities may bring some uncertainties into the validity of Eq. (3). In order to reduce such systematic uncertainties, combined analysis of stripping and pickup data on the same target nucleus

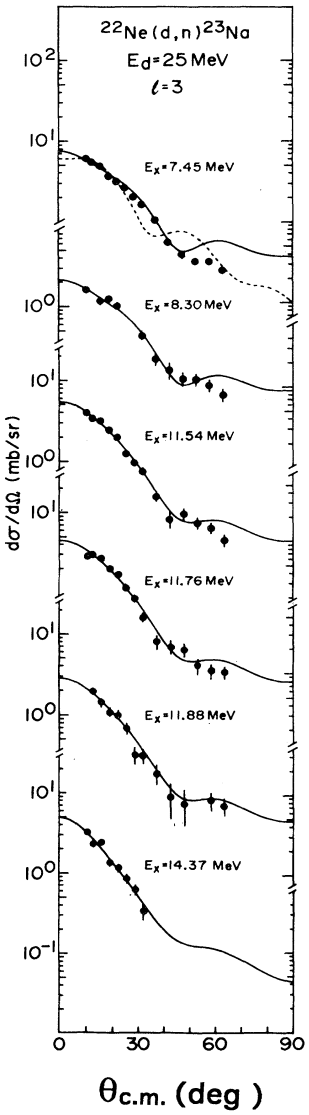


FIG. 10. Differential cross sections for the $l=3$ transitions in the $^{22}$Ne$(d,n)^{23}$Na reaction. Solid lines represent results of the ADBA calculations. For the 7.45-MeV state, the theoretical $l=2$ angular distribution (dashed line) is also shown.

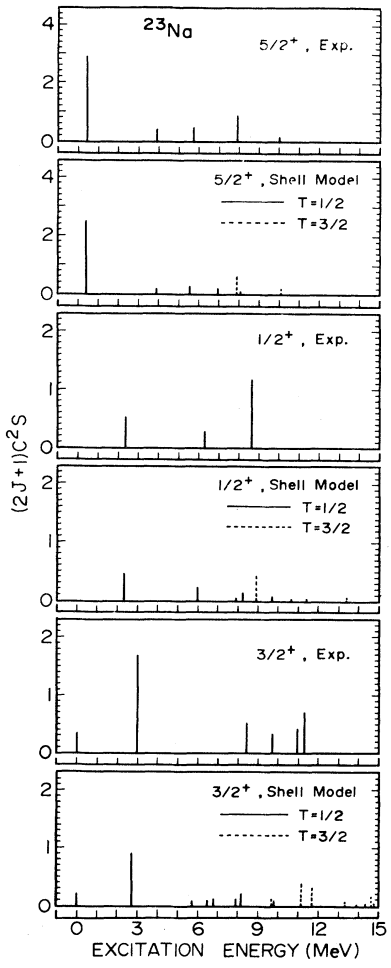


FIG. 11. Comparisons between experimental $2s1d$ strength distributions in $^{23}$Na and shell model predictions.

has recently been carried out [12,13] on the basis of the sum rule Eq. (4). It is plausible to assume that relative spectroscopic strengths are less ambiguous. Therefore, we search for the normalization factors $n^+$ and $n^-$ for the stripping and pickup data, respectively, by evaluating the linear regression so as to simultaneously satisfy Eq. (4) for each $nlj$. In the present analysis, we took the proton pickup data from the $(d,{}^3\mathrm{He})$ reaction on $^{20,22}$Ne at 52 MeV [29,35,36], where almost all the $2s1d$ and $1p$ strengths have been measured. The normalization constants, thus obtained, are $n^+=0.74$, $n^-=1.13$ for $^{20}$Ne and $n^+=0.95$, $n^-=0.80$ for $^{22}$Ne. With the normalizations for $n^+$ and $n^-$, we give the newly defined occupation probability

$$N_{nlj}=\frac{1}{2}\left[\frac{n^-\sum G^-_{nlj}}{2j+1}+1-\frac{n^+\sum G^+_{nlj}}{2j+1}\right]. \tag{5}$$

According to Baranger's definition [38], we evaluate the single-particle energy $E_{nlj}$ from the centroid energy weighted with the stripping and pickup strengths:

$$E_{nlj}=\frac{E^-_{nlj}n^-\sum G^-_{nlj}+E^+_{nlj}n^+\sum G^+_{nlj}}{n^-\sum G^-_{nlj}+n^+\sum G^+_{nlj}}, \tag{6}$$

where

$$E^-_{njl}=-B(A)-\overline{E^-_{nlj}} \tag{7}$$

and

$$E^+_{nlj}=-B(A+1)+\overline{E^+_{nlj}}. \tag{8}$$

$B$ is the ground-state separation energy, and $\overline{E^\pm_{nlj}}$ are the centroid excitation energy evaluated with normalized spectroscopic strengths for the one-nucleon-transfer reactions on the target nucleus $A$. Results of the combined analysis are listed in Table V together with shell model predictions [8]. The obtained occupation probabilities are in accordance with the theoretical ones. Figure 12 shows the distributions of the occupation probabilities of the proton single-particle orbits near the Fermi surfaces of $^{20,22}$Ne. The data are interpreted in terms of the BCS theory. The BCS function is

$$N_{nlj}=\frac{1}{2}\left[1-\frac{(E_{nlj}-\lambda)}{e}\right] \tag{9}$$

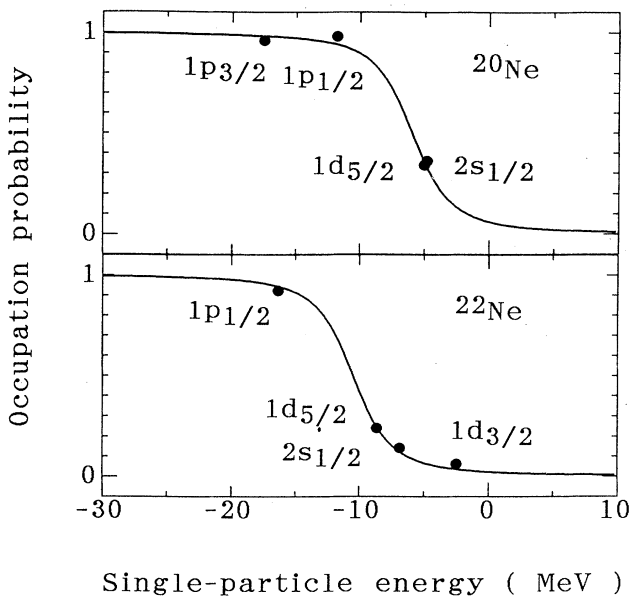


FIG. 12. Distributions of the occupation probabilities of the proton single-particle orbits in $^{20,22}$Ne. Solid lines represent the BCS occupation probabilities.

with

$$e=[(E_{nlj}-\lambda)^2+\Delta^2]^{1/2}. \tag{10}$$

The solid lines in Fig. 12 are the results of the least-squares fit. Obtained gap energies and Fermi energies are

$$\Delta=(3.2\pm0.05)\ \mathrm{MeV}$$

and

$$\lambda=(-6.0\pm0.3)\ \mathrm{MeV\ for\ ^{20}Ne},$$

and

$$\Delta=(3.2\pm0.4)\ \mathrm{MeV}$$

and

$$\lambda=(-10.5\pm0.4)\ \mathrm{MeV\ \ for\ ^{22}Ne},$$

leading to the qualitative conclusion that the effect of the ground-state correlations is similar for the Ne isotopes, and that the Fermi energy increases in magnitude in going from $^{20}$Ne to $^{22}$Ne.

As a conclusion of this part, the occupation probabili-

TABLE V. Occupation probabilities and single-particle energies of the proton orbits in $^{20,22}$Ne.

| | $^{20}$Ne | | | | $^{22}$Ne | | | |
|---|---|---|---|---|---|---|---|---|
| $nlj$ | $n^+\sum G^+_{nlj}+n^-\sum G^-_{nlj}$ | $E_{nlj}$ | $N_{nlj}$ | Shell model[a] | $n^+\sum G^+_{nlj}+n^-\sum G^-_{nlj}$ | $E_{nlj}$ | $N_{nlj}$ | Shell model[a] |
| $1p_{3/2}$ | 3.98 | −17.5 | 0.96 | | | | | |
| $1p_{1/2}$ | 2.30 | −11.8 | 0.98 | | 1.85 | −16.4 | 0.92 | |
| $1d_{5/2}$ | 5.80 | −5.0 | 0.34 | 0.20 | 6.10 | −8.7 | 0.24 | 0.23 |
| $2s_{1/2}$ | 2.30 | −4.8 | 0.36 | 0.26 | 2.23 | −6.9 | 0.14 | 0.21 |
| $1d_{3/2}$ | | | | 0.07 | 3.78 | −2.5 | 0.06 | 0.05 |

[a]Theoretical occupation probabilities of the $2s1d$ shell model (Ref. [8]).

ties and single-particle energies of the proton orbits near Fermi levels in the ground states of $^{20,22}$Ne were deduced in a framework of combined analysis of the stripping and pickup data on the same target nucleus. However, it should be noted that we could not perform a summation up to infinite excitation energy, thus the present results were obtained by the sum of strengths in the valence region.

### D. Higher-order reaction process

The ground states in $^{21,23}$Na are very weakly populated. As shown in Fig. 13, the angular distributions for these $\frac{3}{2}^+$ states exhibit different shapes from those for the strong $1d_{3/2}$ transitions in each case, suggesting that the effect of higher-order reaction processes may be involved in these transitions. An important example of the higher-order reaction process may be the transition leading to the low-lying $\frac{7}{2}^+$ state at $E_x=1.72$ MeV in $^{21}$Na, where the reaction most likely proceeds through the $(d,d')(d,n)$ and/or $(d,n)(n,n')$ processes, and the direct one-step $1g_{7/2}$ transfer is highly unlike those processes.

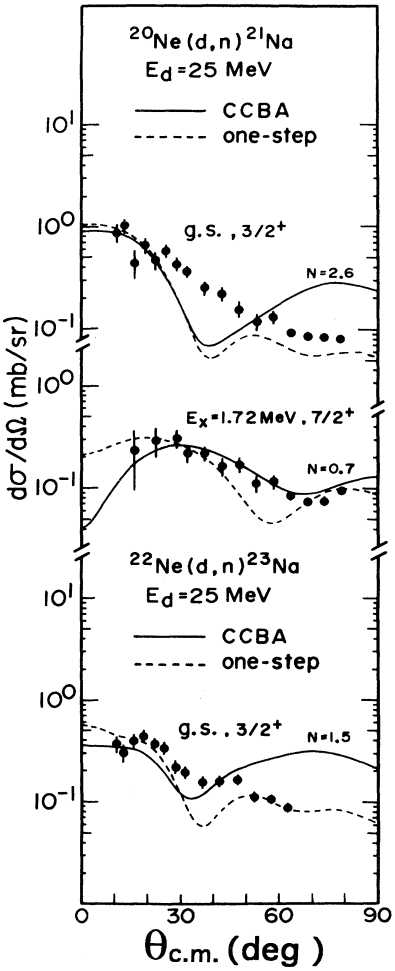


FIG. 13. Differential cross sections for the ground state and 1.72-MeV state transitions in $^{20}$Ne$(d,n)^{21}$Na reaction, and the ground-state transition in the $^{22}$Ne$(d,n)^{23}$Na reaction. Solid lines represent the results of the CCBA calculations and the dashed lines show those of the one-step calculations (ADBA). $N$'s are the normalization factors for CCBA calculations.

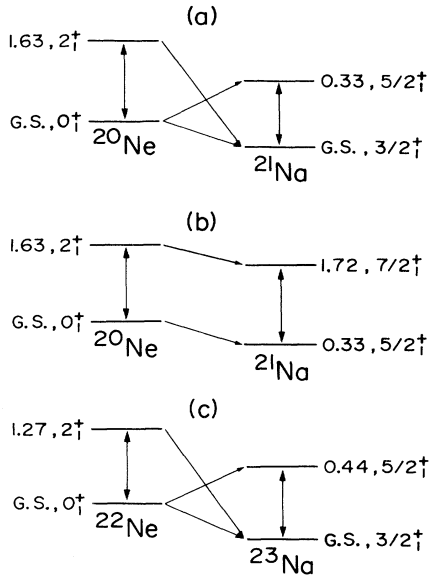


FIG. 14. Coupling schemes used in the CCBA calculations.

We have carried out the coupled-channel Born approximation (CCBA) calculation with the code CHUCK3 [39]

TABLE VI. Deformation parameters and spectroscopic amplitudes used in the two-step calculations.

| Transitions | Spectroscopic amplitude | Deformation parameter | |
|---|---|---|---|
| $^{20}$Ne$(d,n)^{21}$Na | | | |
| $0_1^+ \leftrightarrow 2_1^+$ | | $\beta_2=0.47$ | $\beta_4=0.28$ |
| $0_1^+ \rightarrow \frac{3}{2}_1^+$ | $1d_{3/2}$:−0.17 | | |
| $0_1^+ \rightarrow \frac{5}{2}_1^+$ | $1d_{5/2}$:−0.79 | | |
| $2_1^+ \rightarrow \frac{3}{2}_1^+$ | $1d_{5/2}$:−1.03 | | |
| | $2s_{1/2}$:0.16 | | |
| | $1d_{3/2}$:0.24 | | |
| $2_1^+ \rightarrow \frac{5}{2}_1^+$ | $1d_{5/2}$:0.19 | | |
| | $2s_{1/2}$:0.21 | | |
| | $1d_{3/2}$:0.19 | | |
| $2_1^+ \rightarrow \frac{7}{2}_1^+$ | $1d_{5/2}$:0.90 | | |
| | $1d_{3/2}$:−0.01 | | |
| $\frac{3}{2}_1^+ \leftrightarrow \frac{5}{2}_1^+$ | | $\beta_2=0.47$ | $\beta_4=0.28$ |
| $\frac{5}{2}_1^+ \leftrightarrow \frac{7}{2}_1^+$ | | $\beta_2=0.47$ | $\beta_4=0.28$ |
| $^{22}$Ne$(d,n)^{23}$Na | | | |
| $0_1^+ \leftrightarrow 2_1^+$ | | $\beta_2=0.47$ | $\beta_4=0.28$ |
| $0_1^+ \rightarrow \frac{3}{2}_1^+$ | $1d_{3/2}$:−0.22 | | |
| $0_1^+ \rightarrow \frac{5}{2}_1^+$ | $1d_{5/2}$:−0.65 | | |
| $2_1^+ \rightarrow \frac{3}{2}_1^+$ | $1d_{5/2}$:−0.97 | | |
| | $2s_{1/2}$:0.14 | | |
| | $1d_{3/2}$:0.21 | | |
| $\frac{3}{2}_1^+ \leftrightarrow \frac{5}{2}_1^+$ | | $\beta_2=0.47$ | $\beta_4=0.28$ |

with the coupling scheme shown in Fig. 14. The deformation parameters ($\beta_2$,$\beta_4$) and spectroscopic amplitudes used in the CCBA analysis are listed in Table VI, where $\beta_2$ and $\beta_4$ have been taken from the work by Swiniarski *et al.* [40], and the spectroscopic amplitudes have been obtained from the $2s\,1d$ shell model wave functions [8] using the code OXBASH [25]. In the middle of Fig. 13, the angular distribution of the 1.72-MeV state in $^{21}$Na is shown together with results of the CCBA and ADBA calculations. The $N$'s in the figure are the normalization factors to optimize the fitting for CCBA calculations. It is worth noting that the differential cross sections for the transition to the 1.72-MeV state in $^{21}$Na are well reproduced by the CCBA calculations, while these calculations fail to explain the ground-state transitions as shown in Fig. 13.

## V. SUMMARY

A systematic study of the $^{20,22}$Ne$(d,n)^{21,23}$Na reactions at $E_d=25$ MeV has been made. The proton single-particle properties of the states up to $E_x=15$ MeV were investigated. Differential cross sections were successfully reproduced by the ADBA calculations. The spectroscopic strengths for proton unbound states were deduced by means of the method of Vincent and Fortune.

It was found that in each case most of the proton single-particle strengths were concentrated on the lowest states for the $1d_{5/2}$ and $2s_{1/2}$ orbits, while for the $1d_{3/2}$ orbit its strength was fragmented over several states. The summed spectroscopic strengths for the $2s\,1d$ proton shell almost exhausted the sum-rule limit. These observations were well reproduced by the recent $2s\,1d$ shell model calculations [8]. For the $1f$ strength in $^{21,23}$Na, several $l=3$ transitions have newly been observed in the present measurements.

The combined analysis of the present data and the proton pickup ($d$,$^3$He) data was made in order to obtain the occupation probabilities and single-particle energies of the proton orbits near the Fermi surfaces of $^{20,22}$Ne. The results of the analysis indicates the same amount of ground-state correlations for $^{20}$Ne and $^{22}$Ne.

## ACKNOWLEDGMENT

Authors would like to acknowledge the staff of the Cyclotron and Radioisotope Center for their assistance during running of this experiment.

[1] M. B. Burbank, G. G. Frank, N. E. Davison, G. C. Neilson, S. S. M. Wong, and W. J. McDonald, Nucl. Phys. **A119**, 184 (1968).
[2] F. X. Haas, C. H. Johnson, and J. K. Bair, Nucl. Phys. **A193**, 65 (1972).
[3] Wendell A. Childs, R. C. Ritter, B. D. Murphy, and P. M. Strang, Nucl. Phys. **A203**, 133 (1973).
[4] J. Dubois, Nucl. Phys. **A104**, 657 (1967).
[5] J. R. Powers, H. T. Fortune, R. Middleton, and Ole Hansen, Phys. Rev. C **4**, 2030 (1971).
[6] E. N. M. Quint, B. M. Barnett, A. M. van den Berg, J. F. J. van den Brand, H. Clement, R. Ent, B. Frois, D. Goutte, P. Grabmayr, J. W. A. den Herder, E. Jans, G. J. Kramer, J. B. J. M. Lanen, L. Lapikás, H. Nann, G. van der Steenhoven, G. J. Wagner, and P. K. Ade Witt Huberts, Phys. Rev. Lett. **58**, 1088 (1987).
[7] J. Wesseling, C. W. de Jager, L. Lapikás, H. de Vries, M. N. Harakeh, N. Kalantar-Nayestanaki, L. W. Fagg, R. A. Lindgren, and D. Van Neck, Nucl. Phys. **A547**, 519 (1992).
[8] B. H.Wildenthal, Prog. Part. Nucl. Phys. **11**, 5 (1984).
[9] M. Jaminon, C. Hahaux, and H. Hgô, Nucl. Phys. **A440**, 228 (1985).
[10] S. Fantoni and V. R. Pandharipande, Nucl. Phys. **A247**, 473 (1984).
[11] V. R. Pandharipande, C. N. Papanicolas, and J. Wambach, Phys. Rev. Lett. **53**, 1133 (1984).
[12] A. Pfeiffer, G. Mairle, K. T. Knöpfle, T. Kihm, G. Seegert, P. Grabmayr, G. J. Wagner, V. Bechtold, and L. Friedrich, Nucl. Phys. **A455**, 381 (1986).
[13] S. Khan, G. Mairle, K. T. Knöpfle, Th. Kihm, Liu-Ken Pao, P. Grabmayr, G. J. Wagner, and L. Friedrich, Nucl. Phys. **A481**, 253 (1988).
[14] K. Miura, T. Tohei, T. Nakagawa, A. Sato, T. Ishimatsu, T. Kawamura, K. Furukawa, M. Kabasawa, Y. Takahashi, H. Orihara, T. Niizeki, K. Ishii, and H. Ohnuma, Nucl. Phys. **A467**, 79 (1987); A. Sato *et al.*, CYRIC report, 1985 (unpublished); M. Mori *et al.*, CYRIC report, 1988 (unpublished).
[15] A. Terakawa, D. of Sci. dissertation, Tohoku University, 1993.
[16] H. Orihara and T. Murakami, Nucl. Instrum. Methods **188**, 15 (1981).
[17] H. Orihara, S. Nishihara, K. Furukawa, M. Kabasawa, T. Kawamura, Y. Takahashi, T. Nakagawa, and K. Maeda, Nucl. Instrum. Methods A **257**, 189 (1987).
[18] G. L. Wales and R. C. Johnson, Nucl. Phys. **A274**, 168 (1976).
[19] P. D. Kunz, University of Colorado, computer code DWUCK (unpublished).
[20] F. D. Becchetti and G. W. Greenlees, Phys. Rev. **182**, 1190 (1969).
[21] J. D. Carlson, C. D. Zafiratos, and D. A. Lind, Nucl. Phys. **A249**, 29 (1975).
[22] W. W. Daehnick, J. D. Childs, and Z. Vrcelj, Phys. Rev. C **21**, 2253 (1980).
[23] C. M. Vincent and H. T. Fortune, Phys. Rev. C **2**, 782 (1970).
[24] A. J. Howard, J. G. Pronko, and C. A. Whitten, Jr., Nucl. Phys. **A152**, 317 (1970).
[25] B. A. Brown, W. E. Ormand, and J. S. Winfield, MSU Version of OXBASH82 by A. Etchegoyen, W. D. M. Rae, and N. S. Godwin (unpublished).
[26] P. M. Endt and C. van der Leun, Nucl. Phys. **A310**, 1 (1978).
[27] P. M. Endt, Nucl. Phys. **A521**, 1 (1990).
[28] A. J. Howard, J. G. Pronko, and C. A. Whitten, Jr., Phys. Rev. **184**, 1094 (1969).

[29] G. Mairle, Liu Ken Pao, G. J. Wagner, K. T. Knöpfle, and H. Riedsel, Z. Phys. A **301**, 157 (1981).
[30] H. T. Fortune, J. D. Garrett, and R. Middleton, Phys. Rev. C **19**, 1615 (1979).
[31] J. B. French and M. H. Macfarlane, Nucl. Phys. **26**, 168 (1961).
[32] R. Stock and T. Tamura, Phys. Lett. **22**, 304 (1966).
[33] C. Schmidt and H. H. Duhm, Nucl. Phys. **A155**, 644 (1971).
[34] E. Krämer, G. Marile, and G. Kaschl, Nucl. Phys. **A165**, 353 (1970).
[35] G. Th. Kaschl, G. J. Wagner, G. Mairle, U. Schmidt-Rohr, and P. Turek, Nucl. Phys. **A155**, 417 (1970).
[36] G. Mairle, G. J. Wagner, K. T. Knöpfle, Liu Ken Pao, H. Riedesel, V. Bechtold, and L. Friedrich, Nucl. Phys. **A363**, 413 (1981).
[37] P. Grabmayr, Prog. Part. Nucl. Phys. **29**, 251 (1992).
[38] Michel Baranger, Nucl. Phys. **A149**, 225 (1970).
[39] P. D. Kunz, University of Colorado, computer code CHUCK (unpublished).
[40] R. de Swiniarski, C. Glashausser, D. L. Hendrie, J. Sherman, A. D. Bacher, and E. A. McClatchie, Phys. Rev. Lett. **23**, 317 (1969).